Size-tunable silver nanoparticle synthesis in glycerol driven by a low-pressure nonthermal plasma

Chi Xu[1] , **Himashi P Andaraarachchi**[1], **Zichang Xiong**[1] , **Mohammad Ali Eslamisaray**[1], **Mark J Kushner**[2,]* and **Uwe R Kortshagen**[1,]*

[1] Department of Mechanical Engineering, University of Minnesota, 111 Church Street SE, Minneapolis, MN 55455, United States of America
[2] Department of Electrical Engineering and Computer Science, University of Michigan, 1301 Beal Ave, Ann Arbor, MI 48109-2122, United States of America

E-mail: mjkush@umich.edu and kortshagen@umn.edu

CrossMark

Abstract

Silver nanoparticles (NPs) are extensively used in electronic components, chemical sensors, and disinfection applications, in which many of their properties depend on particle size. However, control over silver NP size and morphology still remains a challenge for many synthesis techniques. In this work, we demonstrate the surfactant-free synthesis of silver NPs using a low-pressure inductively coupled nonthermal argon plasma. Continuously forming droplets of silver nitrate ($AgNO_3$) precursor dissolved in glycerol are exposed to the plasma, with the droplet residence time being determined by the precursor flow rate. Glycerol has rarely been studied in plasma-liquid interactions but shows favorable properties for controlled NP synthesis at low pressure. We show that the droplet residence time and plasma power have strong influence on NP properties, and that improved size control and particle monodispersity can be achieved by pulsed power operation. Silver NPs had mean diameters of 20 nm with geometric standard deviations of 1.6 under continuous wave operation, which decreased to 6 nm mean and 1.3 geometric standard deviation for pulsed power operation at 100 Hz and 20% duty cycle. We propose that solvated electrons from the plasma and vacuum ultraviolet (VUV) radiation induced electrons produced in glycerol are the main reducing agents of Ag^+, the precursor for NPs, while no significant change of chemical composition of the glycerol solvent was detected.

Supplementary material for this article is available online

(Some figures may appear in color only in the online journal)

1. Introduction

Silver nanoparticles (NPs), along with NPs of other noble metals, are extensively used as materials for catalysis, microelectronics, optoelectronics, biomedical applications, conductive pastes, fuel cells, and battery electrodes [1–5]. Their electrical, optical, and chemical properties can be tuned by size, morphology, composition, and local environment. Synthesis of size tunable Ag NPs is critical to many applications for their well-defined optical and chemical properties.

Various methods have been employed to tune Ag NP sizes in conventional colloidal synthesis systems including reaction temperature, type of precursor, precursor concentration, and the type and amount of ligand additives [6–8].

* Authors to whom any correspondence should be addressed.

In this paper, we discuss the less explored method of low-pressure plasma-driven solution electrolysis (PDSE) using a Ag-glycerol electrolyte solution to synthesize Ag NPs with narrow size distributions. This method produces a highly reactive plasma-solution interface with large fluxes of electrons, free radicals, ions, and photons enabling unique chemical transformations [9–12]. NP production is initiated by the reduction of Ag^+ cations, in this case, provided by $AgNO_3$ dissolved in the glycerol. Conventional chemical electrolysis methods typically employ solid electrodes to drive a current through the electrolyte and to provide reducing agents. The synthesis method used here is current free—an electrically floating glycerol droplet is exposed to a low-pressure plasma to provide the reducing agents.

To date, ionic liquids are the most common electrolyte in low-pressure PDSE systems due to their low vapor pressure and highly stable electrochemical window [13–15]. However, the presence of impurities and moisture in ionic liquids can result in poor reproducibility [16]. To address this issue, different from previous low pressure PDSE studies, we selected glycerol, a simple, inexpensive organic solvent with a low vapor pressure, as our electrolyte solvent. Based on its unique properties, glycerol has become a promising solvent in the solution phase synthesis of metal NPs [17–19]. The use of $AgNO_3$ dissolved in glycerol droplets having a large surface-to-volume ratio enhances the transport of plasma activated species to the plasma-liquid interface and into the bulk liquid. A similar approach utilizing microdroplets in atmospheric pressure PDSE previously demonstrated tight control over the early stage of NP formation [20].

In this work, we report size tuning strategies of Ag NPs in a droplet-based low pressure PDSE system by manipulating precursor residence time, plasma power, and plasma generation waveforms. With shorter droplet exposure to the plasma, the formation of large NPs can be minimized. Pulsed power modulation reduces plasma exposure during a pulse to a few ms, comparable to the diffusion time of electrons from the bulk plasma to the droplet. Electrons entering the droplet rapidly solvate and are consumed in reduction reactions with Ag^+. This temporal control of electron fluxes allows control of the Ag atom inventory in the plasma-liquid interface layer and the balancing of NP growth with diffusion transport of NPs out of the interface layer. Measurements of the lack of change of the chemical composition of glycerol after plasma exposure suggests that solvated electrons originating from the plasma or from photoionization by vacuum ultraviolet (VUV) photons at plasma-liquid interface play a major role in Ag^+ reduction, likely dominating over reducing species generated by glycerol decomposition.

2. Description of the experiment and model

2.1. Experimental methods

Silver NPs were synthesized and collected in a nonthermal radio frequency (RF) inductively coupled plasma reactor. A schematic of the experimental setup is shown in figure 1. As listed in table 1, the discharge gas, Argon, was flowed at
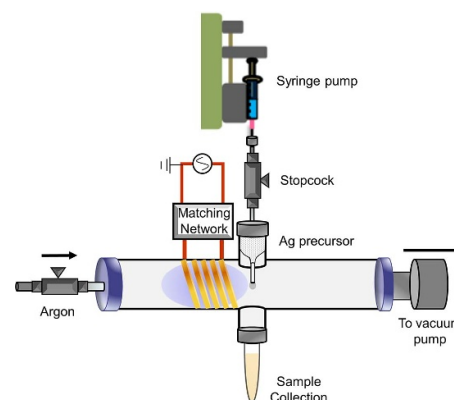
Figure 1. Schematic of plasma-driven electrolysis reactor for synthesis of silver NPs in glycerol. An inductive discharge was produced by a RF power supply that is coupled to a five-turn induction coil through a matching network. $AgNO_3$ solution was delivered with a syringe pump which connected to a quartz pipette with a 1 mm tip. The continuously growing $AgNO_3$-glycerol droplets were in direct contact with the plasma and held by surface tension until they break off into single droplets that are collected.

Table 1. Typical plasma operating conditions in this study.

Ar flow rate (sccm)	80
$AgNO_3$ precursor concentration (mM)	10
Precursor flow rate (ml h^{-1})	9
Upstream pressure (Torr)	5
RF nominal power (W)	60
Plasma radius (cm)	1.10
Collection time (min)	15

80 sccm (standard cubic centimeters per minute) through a 2.54 cm outer diameter and 2.20 cm inner diameter quartz tube with the total pressure in the plasma region being 5 Torr. A plasma was generated by the application of RF power at 13.56 MHz from a power generator through a five turn copper induction coil, coupled with a matching network (HFT1500, Vectronics). The RF power generator consisted of a B&K Precision 4063 arbitrary function generator that created a driving signal with a peak-to-peak voltage between 300 and 620 mV (peak-to-peak), which was fed into an E&I A300 broadband power amplifier (56 db gain). A quartz pipette with 1 mm tip was positioned in the plasma reactor tube through a Swagelok vacuum fitting with its other end connected by polytetrafluoroethylene spaghetti tubing to a syringe pump (NE-300, New Era Pump Systems) as the supply of glycerol.

Silver nitrate solutions were prepared by mixing silver nitrate American Chemical Society (ACS) reagent, ⩾99.0%, Sigma-Aldrich) and glycerol (ACS reagent, ⩾99.5%, Sigma-Aldrich) followed by 1 h sonication. After loading the solution into the syringe pump, several purges were performed by controlling the vacuum pump and three-way stopcock to prevent bubble generation while running the plasma. By continuously operating the syringe pump, $AgNO_3$-glycerol droplets were generated hanging at the pipette tip which was located which was located on the centerline of the quartz tube and axially 8 mm away from the end of the induction coil. This is the default droplet location. While being exposed to the plasma,

Ag-glycerol droplets grew through injection of solution from the syringe pump until the surface tension was insufficient to hold the droplet to the pipette tip. At that time, the droplets separated from the tip and fell into a culture tube for future characterization. The droplet residence time was varied by changing the syringe pump rate.

For qualitative information about NP size and concentration, ultraviolet–visible (UV–Vis) absorption measurements were carried out on a Cary 7000 spectrophotometer. The spectra of as-synthesized Ag-glycerol colloidal samples were recorded at room temperature in a 1 cm quartz cuvette. All spectra were taken immediately after plasma treatment.

Purified Ag NPs were characterized by transmission electron microscopy (TEM) and x-ray diffraction (XRD). Ag NPs were purified by washing with ethanol three times and centrifugation at 14 000 rpm for 1 h. The final product was dispersed in ethanol for further characterization. TEM was conducted on a Tecnai T12 microscope with an accelerating voltage of 120 kV. High-resolution TEM (HRTEM) was performed on a Thermo Fisher Talos F200X microscope with an accelerating voltage of 200 kV. TEM samples were prepared by drop casting a Ag-ethanol solution onto carbon-coated copper grids and were dried in the dark. Particle dimensions were manually measured using the open domain scientific image analysis software ImageJ for sizing more than 300 particles. Mean sizes (diameters) are reported along with geometric standard deviations.

XRD data were recorded with a Bruker D8 Discover 2D x-ray diffractometer with a Co x-ray point source ($\lambda = 1.79$ Å). The XRD patterns were converted to the wavelength of a Cu source ($\lambda = 1.54$ Å) for data analysis. The crystallite sizes were determined from the XRD peak broadening using the Scherrer equation analysis within the XRD analysis software MDI/JADE with a shape factor of $K = 0.89$ [21].

Dynamic light scattering (DLS) measurements were conducted with a Microtrac NanoFlex *in-situ* analyzer in volume distribution mode to measure hydrodynamic diameters of Ag NPs. This instrument was calibrated with National Institute of Standards and Technology (NIST)-traceable particle size standards, and the measured mean diameter has an accuracy of within 5%.

Fourier transform infrared (FTIR) spectra were measured on a Bruker ALPHA FTIR spectrometer using the attenuated total reflection module in a nitrogen-filled glovebox. As-synthesized samples were drop-casted onto the ATR crystal for measurement.

A colorimetric aldehyde assay kit, blue (Sigma-Aldrich MAK140), was used to detect the concentration of aldehyde in glycerol before and after plasma treatment. Presence of aldehydes results in a colorimetric product at 620 nm that can be used to quantify the concentration of aldehydes. The method of measurement and calculation is described in the Sigma-Aldrich technical bulletin [22].

The *p*H measurements were carried out on an Orion Star A215 meter with an Orion PerpHecT ROSS Combination *p*H Microelectrode at room temperature. Before each measurement, the electrode was calibrated with standard *p*H 4.01, 7.00 and 10.01 buffers.

Basic plasma parameters, electron temperature (T_e) and positive ion density (n_i), were measured using a home-made double Langmuir probe. The cylindrical axis of the probe was aligned with the centerline of the reactor tube. Tungsten tips of 10 mm length and 0.075 mm diameter were used. *I–V* characteristics were measured by a source meter (Tektronix 2450, Tektronix, USA) connected to the double probe. Electron temperatures were extracted from *I-V* curves as reported in the literature [23] by assuming that the electron energy distribution is a Maxwellian. Ion densities were computed from *I-V* curves using the Modified Talbot and Chou collisional probe theory [24, 25]. The plasma was assumed to be quasi-neutral so that the electron density equals the positive ion density.

2.2. Description of the plasma reactor model

The plasma reactor was modeled using the hybrid plasma equipment model (HPEM), described in detail in [26–28]. Briefly, the HPEM is a 2-dimensional plasma-hydrodynamics modeling platform that addresses different classes of transport and reactivity in different modules, exchanging information in an iterative, time-slicing fashion. In this investigation, the following modules were used: electromagnetics module (EMM), electron Monte Carlo simulation (EMCS), fluid-kinetics-Poisson module (FKPM) and the radiation transport module (RTM). Separate continuity, momentum and energy equations for each species in the plasma are integrated in time in the FKPM. Poisson's equation is solved for the electrostatic potential using a semi-implicit technique. The electron temperature is obtained from an implicit solution of the energy transport equation, using rate and transport coefficients obtained from stationary solutions of Boltzmann's equation for the electron energy distribution. The frequency domain wave equation is solved in the EMM for the inductively coupled electric fields launched into the plasma from the antenna (coil). Secondary electron emission from surfaces is addressed using the EMCS.

Radiation transport is addressed in the RTM. The technique is described in detail in [28]. In the RTM, pseudo-particles representing photons are isotropically emitted from locations weighted by the density of the emitting excited states, which are assigned a frequency randomly selected from the Voight lineshape function for the state. The trajectory of the photon pseudo-particle is followed until being absorbed in the lineshape function of atoms in the lower state, the photon is absorbed in a photo-ionization or the photon leaves the plasma. The energy of the resonantly reabsorbed photon is quenched if a collision eliminating the excited state occurs during the optical lifetime of the excited state. If not, the photo is re-emitted using partial frequency distribution. This process is continued until the photon leaves the system, is it non-resonantly absorbed or its energy is quenched by collisions.

Simulations were performed in pure argon using the reaction mechanism described in [27]. Radiation transport was computed for the Ar(1s$_3$) $\rightarrow$ Ar ground state resonance transition at 104.8 nm and the Ar(1s$_5$) $\rightarrow$ Ar transition at 106.7 nm. The Ar$_2$* dimer radiation at 121 nm was included in early calculations to confirm that its contribution to the VUV flux at the

position of the droplet was negligible, and was not included in the final calculations presented here. The algorithms used in the RTM and the optical parameters used in the calculation here are discussed in detail in [28].

3. Production of Ag NPs in glycerol droplets

3.1. Size control of silver NPs in continuous wave (CW) plasma operation

Size control of silver NPs was investigated in three sets of experiments by adjusting the silver nitrate concentration, droplet residence time, and plasma discharge parameters. NP formation was monitored by UV–Vis absorption spectroscopy. As a control experiment, to confirm that there is no spontaneous reaction between glycerol and $AgNO_3$ that might produce NPs, an absorption spectrum of 10 mM $AgNO_3$-glycerol solution was taken after 48 h of solution preparation and storage in the dark to prevent any possible photo-induced reactions, as is shown to be important in our discussion in section 3.2 below.

To investigate the effect of $AgNO_3$ concentration on NP formation, the concentration was varied from 3 mM to 10 mM, while keeping a constant precursor flow rate of 9 ml h^{-1}, corresponding to a droplet residence time of 4 s. The plasma was maintained with CW power of 60 W. The transparent precursor solution turned yellow after plasma treatment indicating the formation of Ag NPs (figure S1). The UV–Vis spectra of plasma-treated $AgNO_3$-glycerol solution with different initial concentrations are shown in figure 2(a). The surface plasmon resonance (SPR) peak around 420 nm, which is characteristic for the formation of silver NPs, confirmed that Ag^+ reduction occurs by plasma treatment. Emanov and Chumanov reported on an experimental study of the spectral extinction, i.e. the sum of absorption and scattering, of highly size-controlled colloidal silver NPs with diameters ranging from 29 to 136 nm [29]. They found a nearly linear relationship between extinction cross section and particle diameter and a slow red-shift of the SPR peak from ∼420 nm at 29 nm diameter to ∼440 nm at 61 nm diameter. While no measurements for particles smaller than 29 nm were reported, we assumed that a similar behavior may be extrapolated to smaller diameters. In particular, we assumed that with increasing precursor concentration, as no peak shift is observed, the increase in SPR intensity is directly related to an increase in NP concentration according to the Beer–Lambert law. Hence, we conclude that enhanced Ag^+ ion reduction at higher precursor concentrations leads to a larger Ag NP concentration rather than Ag NPs of larger diameter.

To investigate the effect of droplet residence time, the flow rate of the precursor was varied by operating the syringe pump with a constant precursor concentration of 10 mM. The UV–Vis spectra of as-synthesized samples at different flow rates of 9 ml h^{-1} (4 s residence time) and 3 ml h^{-1} (12 s residence time) are shown in figure 2(b). With longer droplet residence time, the SPR bands were significantly broadened, indicating polydispersity of the particle size distribution [30, 31]. A red shift of SPR peaks from 422 nm to 425 nm occurred with increasing residence time indicating a change in particle
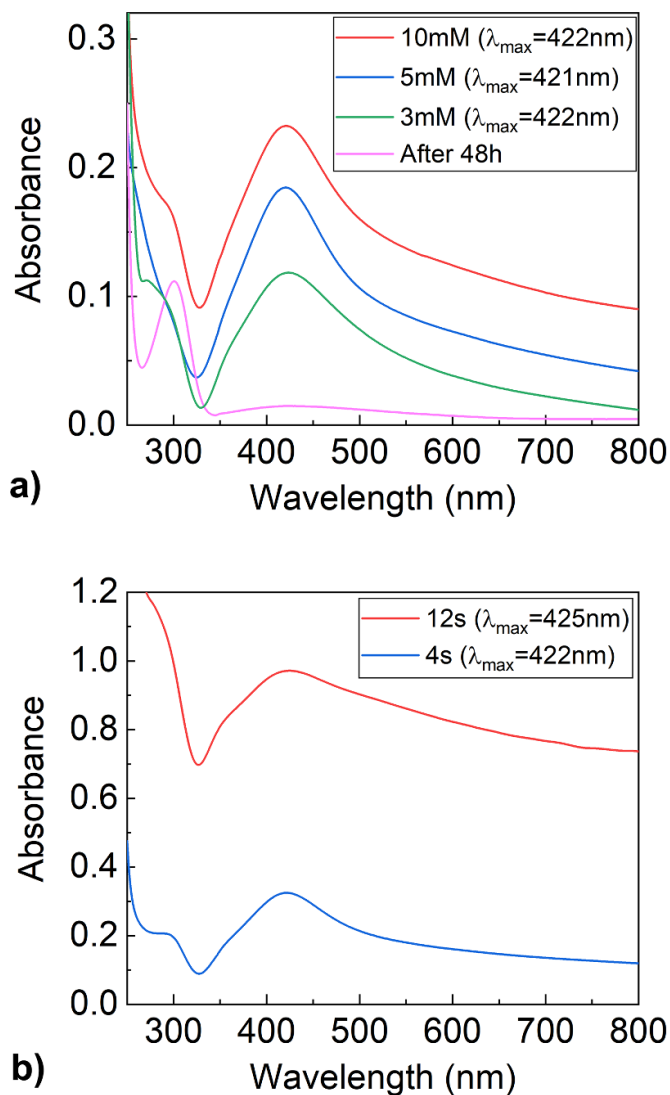
Figure 2. (a) UV–Vis spectra of plasma-treated $AgNO_3$-glycerol dispersions with varying concentrations at the same flow rate. The peak intensity increased with increasing precursor concentration in the studied range. For each curve, the wavelength in the brackets indicates the peak wavelength of the spectrum. (b) UV–Vis spectra of plasma-treated $AgNO_3$-glycerol dispersions illustrating the effect of precursor residence time with a fixed initial concentration of 10 mM.

size. TEM images of Ag NPs at 12 s and 4 s residence times, respectively, are shown in figures 3(a), (b) and (d). With the longer residence time of 12 s, we observed large, irregular shaped Ag NPs with diameters of ∼50 nm interspersed with a large concentration of smaller Ag NPs. The size distribution can be approximated by a log-normal distribution with a geometric mean of 21.7 nm and a geometric standard deviation of 1.8. In comparison, for the shorter residence time of 4 s, we observed spherical Ag NPs with a geometric mean diameter of 20.1 nm and a geometric standard deviation of 1.6, indicative of reduced size dispersity, as shown in figures 3(c) and (g). We suggest that with extended droplet residence time, the continuous reduction of silver ions leads to continued nucleation of Ag NPs that can coalesce and increase in size through
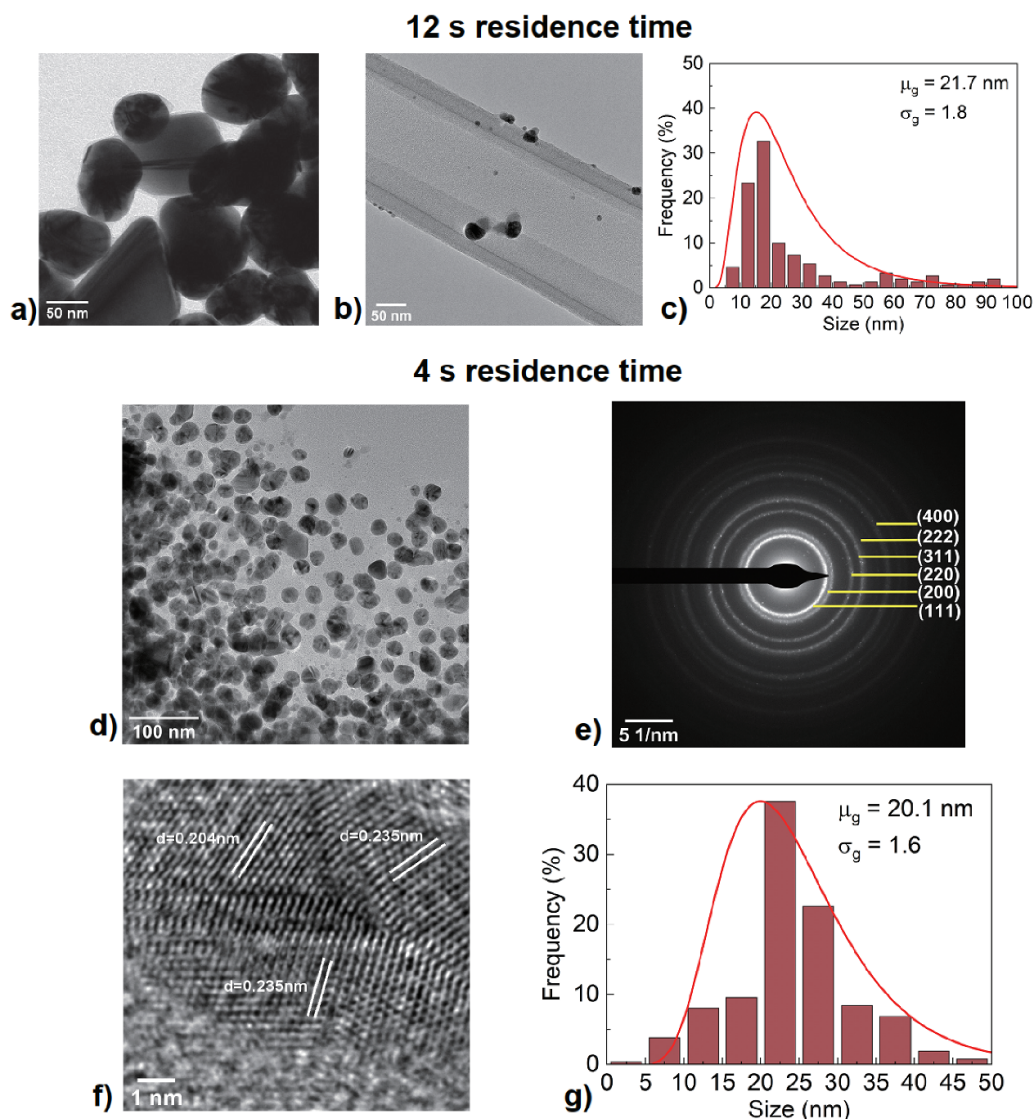
Figure 3. (a), (b) TEM images of synthesized silver NPs at AgNO$_3$ initial concentration of 10 mM, constant power of 60 W and droplet residence time of 12 s. (c) Particle size (diameter) distribution histogram of Ag NPs determined by TEM micrographs. (d) TEM images of synthesized silver NPs at AgNO$_3$ initial concentration of 10 mM, constant power of 60 W and droplet residence time of 4 s. (e) SAED pattern of randomly selected Ag NPs. (f) HRTEM image of the same sample showing lattice fringes for the (111) and (220) plane. (g) Particle size (diameter) distribution histogram of Ag NPs.

surface growth, leading to large particles with a broad size distribution.

Selected area diffraction pattern (SAED) of these Ag NPs in figure 3(e) were assigned to (111), (200), (220), (311), (222) and (400) planes of face-centered cubic (fcc) silver phase (JCPDS 04-0873). For a residence time of 4 s, oval shaped Ag NPs with grain boundaries were observed, which indicates that particles were formed by the coalescence of smaller NPs. A typical HRTEM image exhibiting a crystalline structure with a *d*-spacing of 0.235 nm and 0.204 nm is shown in figure 3(f), which correspond to the (111) and (200) planes of the fcc phase Ag NPs, respectively. The energy dispersive x-ray spectroscopy (EDS) spectrum shows Ag peaks, which further confirmed the particle composition (figure S2). The XRD pattern in figure S3 exhibits three diffraction peaks at 2θ values of 38.11°, 44.21°, 64.39° corresponding to the (111), (200) and (220) lattice planes of fcc structure of Ag, respectively.

These results suggest that adjusting the droplet residence time is an effective way of controlling the size of Ag NPs under CW plasma operation.

### 3.2. Influence of plasma charge carrier density and VUV fluxes

To investigate the effect of plasma parameters on Ag NP growth, we first carried out double Langmuir probe measurement to obtain the electron temperature (T_e) and positive ion density (n_i) along the axis of the reactor. Since VUV photons may also have an influence on Ag NP formation but are difficult to assess experimentally inside the plasma, VUV fluxes were evaluated through plasma simulation.

For the interpretation of the probe measurements, the plasma is assumed to be quasineutral such that the electron density n_e is equal to n_i. To replicate typical operating

a)
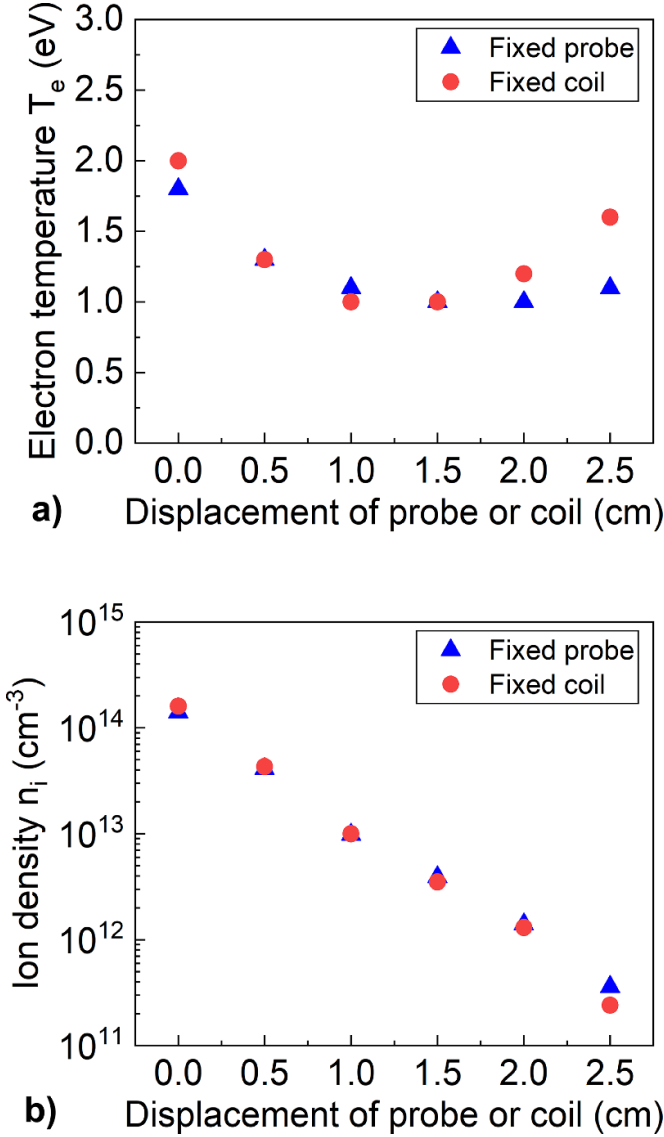
Figure 4. (a) Electron temperature and (b) electron density in the argon discharge. The measurements were taken by either fixing the probe and moving the induction coil or moving the probe while fixing the coil. The measured T_e and n_i at the location of precursor droplet were about 1.9 eV and 1.5×10^{14} cm^{-3}, respectively.

conditions, 80 sccm Ar was flowed through the reactor with an upstream pressure of 5 Torr. Measurements were performed by either moving the induction coil and fixing the probe or moving the probe while keeping the induction coil at the closest location to the droplet. Here, z represents the displacement of the induction coil or probe with respect to the default droplet location. At a nominal power of 60 W, the electron temperature measured by the probe was around 2 eV at the position of the default droplet location ($z = 0$ cm) and decreased downstream of the coil, as shown in figures 4(a) and (b). The electron (ion) density at $z = 0$ cm was about 1.5×10^{14} cm^{-3} and decreased almost exponentially downstream of the induction coil, dropping by about one order of magnitude per cm. Small differences at larger probe-coil distances are likely due to different coupling of the plasma to upstream metal parts when the probe is moved compared to when the coil is moved.

b)
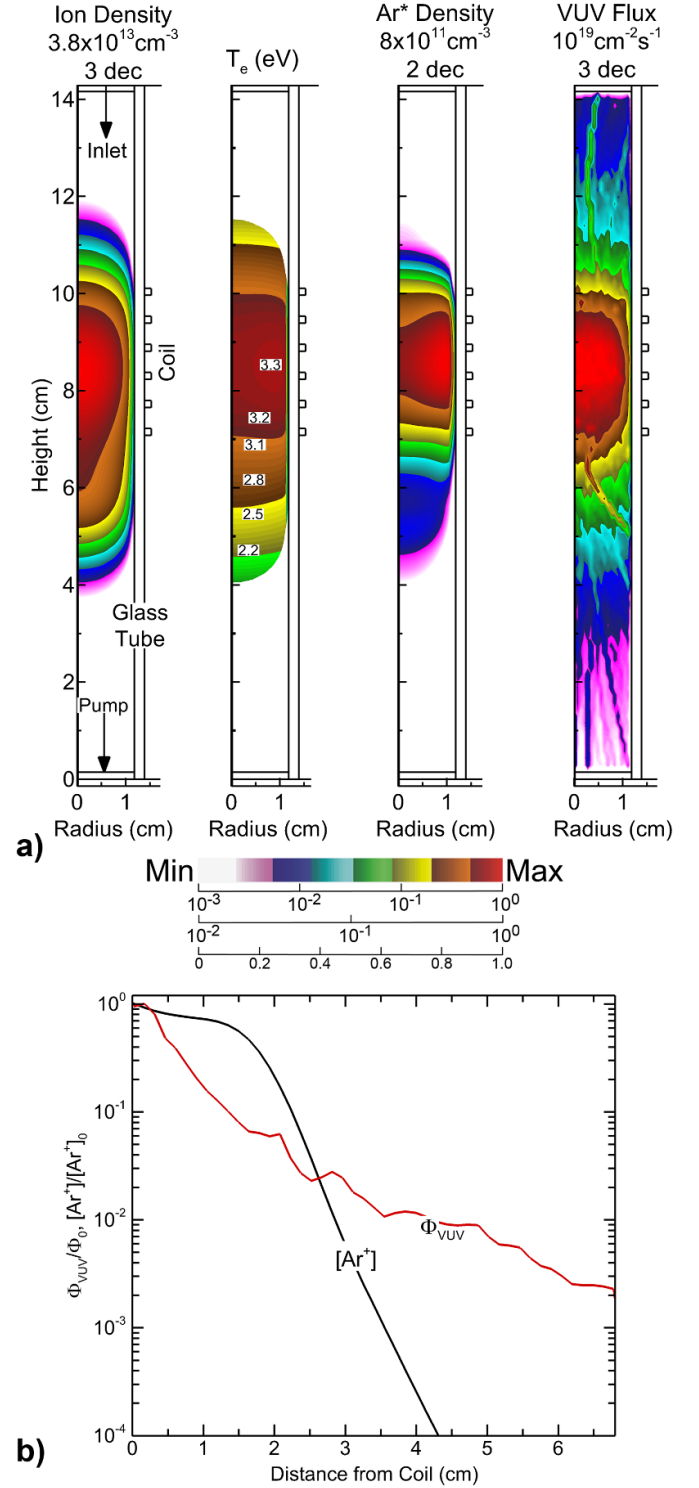
Figure 5. Computed plasma properties for a discharge of 80 sccm Ar with a pressure of 5 Torr at 60 W power. (a) Ion density, electron temperature, radiating excited state density and VUV flux. The ion density n_i drops fast, using a log-scale over three decades, from a maximum of 3.8×10^{13} cm^{-3}. (b) Ion density and VUV flux on the axis normalized by the value at the bottom of the coils.

The results of the double probe are qualitatively consistent with the simulation results in figure 5(a) for the same conditions. In particular, the simulation reflects the rapid
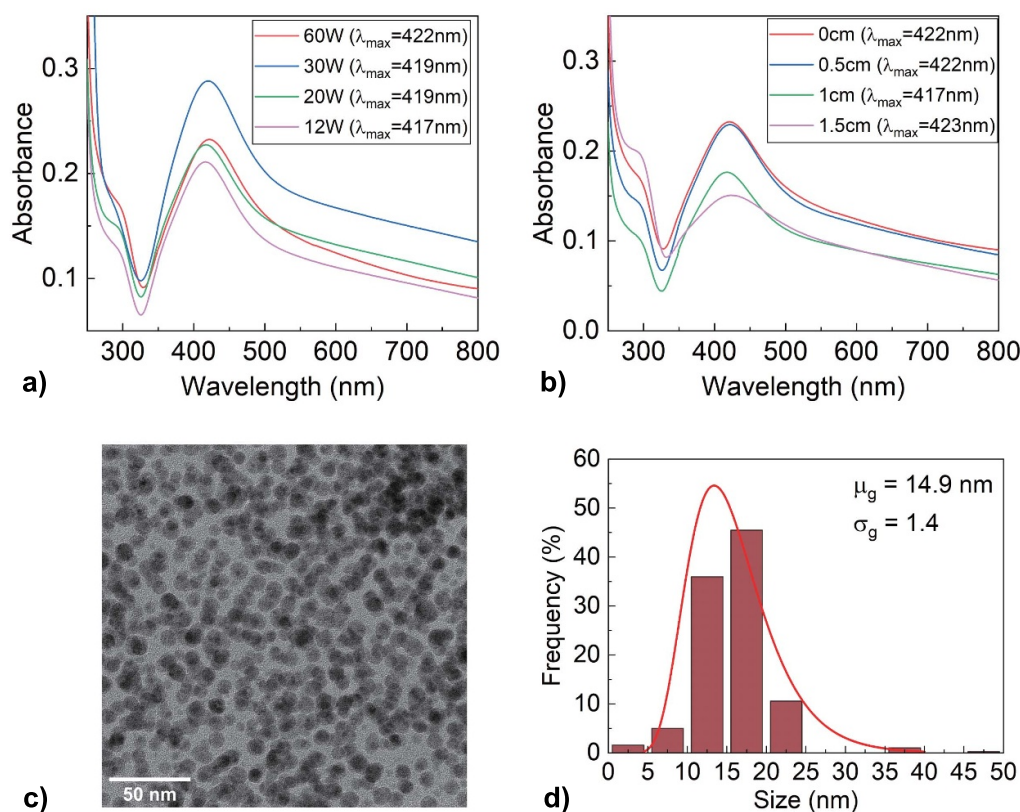
Figure 6. (a) UV–Vis spectra of plasma-treated $AgNO_3$-glycerol dispersions with varying plasma power for an $AgNO_3$ initial concentration of 10 mM and residence time of 4 s. (b) UV–Vis spectra of plasma-treated $AgNO_3$-glycerol dispersions of NPs illustrating the effect of VUV flux with different distances between induction coil and droplet. (c) TEM images and (d) particle diameter distribution histogram of synthesized silver NPs with a $AgNO_3$ initial concentration of 10 mM, plasma power of 12 W and 4 s residence time.

axial decay of the electron density observed with the double probe but predicts a much slower axial decay of the VUV fluxes, as shown in figure 5(b). While the simulation predicts a higher electron temperature than measured with the probe, this is likely due to the assumptions that need to be made in interpreting double probes measurements, which provide an effective electron temperature for non-Maxwellian electron energy distribution functions (EEDFs). For a symmetric double probe, both probes operate around their floating potential [23] and thus only sample the energetic electrons in the tail of the EEDF, which at the pressure used in our experiments are expected to have a lower temperature than the electron temperature characteristic of the bulk of the EEDF.

To study the effect of varying electron and VUV fluxes, we first changed the plasma input power at a constant precursor concentration of 10 mM and a droplet residence time of 4 s. As shown in figure 6(a), when plasma power was increased from 12 W to 30 W, leading to increasing electron and VUV fluxes, a red shift of SPR peak (417–422 nm) was observed indicating an increase of the Ag NP size. This observation agrees well with the TEM images and size distributions shown in figures 6(c), (d) and S4, for NPs produced with increasing plasma powers. Increasing plasma power leads to an increasing density of reducing species, including solvated electrons, resulting in more Ag^+ reduction, more nucleation followed

by particle growth through surface reactions or coalescence. However, it is possible that with higher plasma powers (e.g.: 60 W), surface reactions dominate particle growth forming larger but fewer Ag NPs exhibiting a less intense, red-shifted SPR peak. Decreasing plasma power from 60 to 12 W decreases the geometric standard deviation of the particles from 1.6 to 1.4, with smaller geometric mean diameter of 14.9 nm.

As indicated by the simulation results in figure 5(b), another way to tune electron and VUV fluxes to the precursor droplet is to change the distance between the plasma and droplet by moving the induction coil (increasing z). If plasma electrons are the source of the main reducing species, one would expect a significant decrease in Ag NP yield by moving the induction coil away from the default location, as predicted by the results in figures 4(b) and 5(a). However, the UV–Vis spectra in figure 6(b) show a much weaker decay of the SPR peak with increasing distance of the droplet from the plasma without a significant shift in peak wavelength. TEM images in figure S5 (supplementary information) also show that there is no significant decrease in particle size. To explain these observations, we note that the VUV flux predicted by the plasma simulation in figure 5(b) decreases slower than electron density (electron flux) in the axial direction. VUV flux mostly from Ar^* monomers, extends towards the afterglow region all the way to the downstream end of the tube, as shown in figure 5(a). Since photoionization of glycerol for photon energies of 9–12 eV can

J. Phys. D: Appl. Phys. **55** (2022) 015201

C Xu *et al*

lead to precursor fragmentation [32, 33], we propose that the reducing ability of electrons and precursor radicals generated by VUV ionization of glycerol is not negligible.

3.3. Influence of pulsed plasma power

Pulsed power operation can be used to modulate the electron and VUV fluxes incident onto the surface of the droplet. If the diffusion time for electrons from the plasma to the droplet is shorter than the pulse period, then there will be discrete pulses of electrons solvating into the droplet and VUV fluxes incident onto the droplet. Since the lifetime for solvated electrons in the droplet is much shorter than the pulse periods used here, pulsing the plasma also produces pulses of a finite amount of Ag^+ reduction in the droplet producing a finite pulse of Ag^0. To investigate these processes, the CW power of 60 W was modulated using a function generator. Neglecting pulse rise and fall times, the pulsed power is described by

$$P(t) = \begin{cases} P_0, \; 0 \leqslant t < \eta\tau \\ 0, \; \eta\tau \leqslant t < \tau \end{cases}, \qquad (1)$$

where η (between 0% and 100%) is the duty cycle for the plasma-on time and τ is the pulse period. In the following cases, $P_0 = 60$ W while the pulse frequency $f = 1/\tau$. Duty cycle was 20% for all the reactions reported below. This means that the time averaged power during pulsing was 12 W.

The UV–Vis absorption spectra of Ag NPs synthesized with a droplet residence time of 4 s, 10 mM precursor concentration, and pulse frequencies of 10 and 100 Hz are shown in figure 7. Pulse modulation has a significant effect on Ag NP growth. The SPR peak intensity is larger and with pulsing than under CW conditions. From CW excitation to $f = 100$ Hz, the SPR band increased in intensity and narrowed. TEM images and size distributions for 10 Hz and 100 Hz pulse frequencies are shown in figures 7(b)–(e). For 10 Hz, the geometric mean size is 9.1 nm with a geometric standard deviation of 1.3. For 100 Hz, the geometric mean size decreases to 5.6 nm with a geometric standard deviation of 1.4. For both frequencies, the size distributions are narrower than for CW operation which produces a geometric standard deviation of 1.6. The hydrodynamic diameters of these Ag NPs measured by DLS are 9.0 nm at 10 Hz and 7.4 nm at 100 Hz, as shown in figure S6, consistent with TEM results. These results demonstrate that pulsed power for these conditions reduces the particle size and leads to more narrow size distributions of Ag NPs.

The rate of loss of electrons and ions during the afterglow of a pulsed argon plasma at 5 Torr is dominated by ambipolar diffusion. At 5 Torr pressure, electrons rapidly thermalize during the afterglow to a temperature of about 0.3–0.1 eV [34, 35]. The resulting ambipolar diffusion coefficient is approximately $D_A = D_I(1 + T_e/T_I)$, where D_I is the free diffusion coefficient of the argon ion, T_I is ion temperature and T_e is electron temperature. For a diffusion length of Λ, the time for decay of the plasma by diffusion is

$$\tau_d = \Lambda^2/D_A. \qquad (2)$$
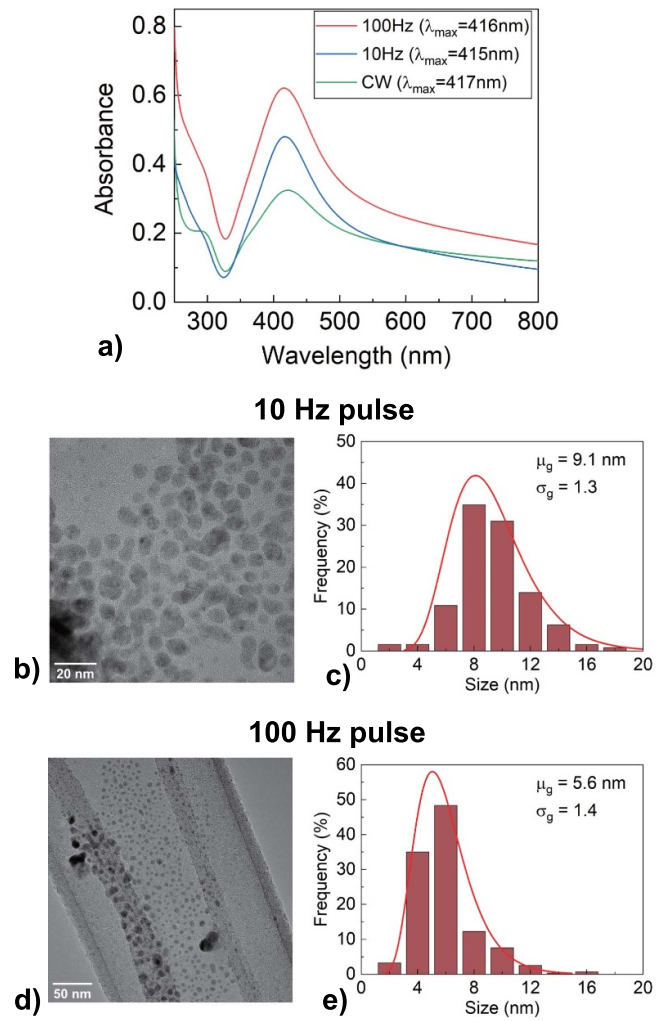
Figure 7. (a) UV–Vis spectra of plasma-treated AgNO$_3$-glycerol dispersions with varying modulation frequency of the applied power with a duty cycle of 20%. The precursor concentration and residence time remained at 10 mM and 4 s. Nanoparticle concentration increased while the diameter distribution narrowed as a result of pulse modulation. (b) TEM images and (c) particle size distribution histogram of synthesized silver NPs with a AgNO$_3$ initial concentration of 10 mM and 4 s residence time. The pulse modulation frequency was 10 Hz. (d) TEM images and (e) size distribution of synthesized silver NPs at AgNO$_3$ initial concentration of 10 mM and 4 s residence time. The pulse modulation frequency was 100 Hz.

The reduced mobility μ_0 (normalized to standard pressure and temperature) for argon ions at low E/N is 1.53 cm^2 (V s)$^{-1}$ [36], which corresponds to a diffusion coefficient at 5 Torr and ion temperature of 0.03 eV of $D_I = 7.7$ cm^2 s^{-1}. The radial diffusion length of cylindrical tube having a diameter of 2.20 cm is $\Lambda = 0.46$ cm, giving a diffusion decay time of 6.3 ms. With the interpulse period for both 10 Hz and 100 Hz modulation frequency being longer than the diffusion decay time, plasma electrons have largely recombined during the plasma-off period.

These trends were confirmed by modeling of the pulsed plasma. Results from the model show that following termination of the power at 100 Hz, the electron temperature
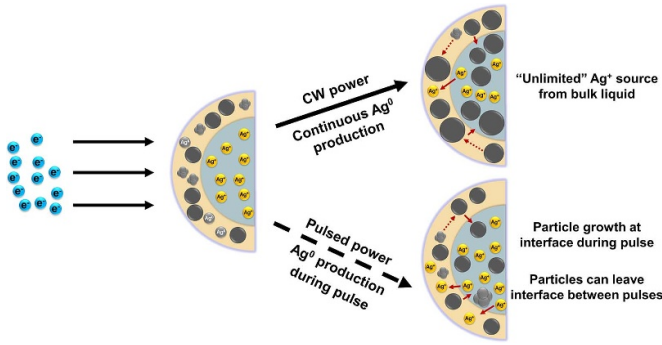
Figure 8. Schematic of evolution of Ag NPs with different size control strategies during plasma treatment. With continuous power treatment, the bulk liquid (blue region) acts as a continuous source of Ag^+, which enables solvating electrons to generate Ag^0 atoms for nucleation and surface growth in the interface region. In comparison, during the plasma-off period of pulsed operation, reduction processes no longer dominate in the interface region (yellow shell) which further prevents the formation of large particles.
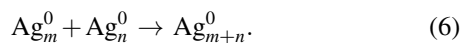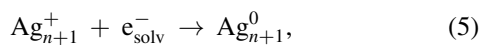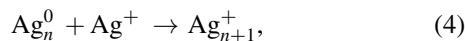
decreases from 3 eV to 0.3 eV within 0.5 ms. During this time, the ion density decreases by a factor of about 2. The ion density then decays by ambipolar diffusion and recombination on the walls by a factor of 10^4 in the next 8 ms before the next pulse while the electron temperature thermalizes to nearly the gas temperature.

Based on the solvation and decay times of electrons in glycerol being on the order of hundreds of nanoseconds or less [37], much shorter than the electron decay time in the plasma, we can construct a scenario for the pulsed power production of NPs. Similar to established reaction mechanisms in water and ethylene glycol [38–41], we propose the following reactions in glycerol that govern the NP growth dynamics with and without pulse power modulation.

As illustrated in figure 8, we suggest that during the plasma-on period, Ag^+ ions are reduced to Ag atoms by solvated electrons from the plasma or those produced in the droplet by VUV radiation,

$$e^-_{solv} + Ag^+ \rightarrow Ag^0. \tag{3}$$
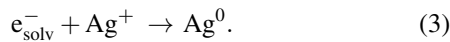
When the plasma is turned off, this reduction reaction quickly ceases due to the decrease in both the reducing electron density and the VUV radiation. For these pulsed conditions, a finite pulse or inventory of Ag^0 atoms is produced. This finite inventory then enters into a sequence of reactions resulting in the nucleation of Ag clusters and their coalescence leading to the formation of Ag NPs,

$$Ag^0_n + Ag^+ \rightarrow Ag^+_{n+1}, \tag{4}$$

$$Ag^+_{n+1} + e^-_{solv} \rightarrow Ag^0_{n+1}, \tag{5}$$

$$Ag^0_m + Ag^0_n \rightarrow Ag^0_{m+n}. \tag{6}$$

Since there is a finite inventory of Ag^0, this sequence of reactions terminates before large clusters are formed that

would then have coalesced to produce larger NPs. The results in table 2 for NP sizes for pulsed and CW power suggest that nucleation dominates over particle coalescence and growth in the pulsed power mode. With CW power at 12 W, the same average power as for pulsing, NP sizes are larger. The continuous availability of reducing electrons and production of Ag^0 during CW operation enables reduction of larger cluster ions Ag^+_n (reaction 5) and surface growth reactions (reaction 6) that are not available with the finite pulse of Ag^0 produced with pulsed power.

Compared to aqueous solutions, nucleation and coalescence are inhibited due to the lower rates of diffusion of Ag monomers and clusters in glycerol [42, 43]. The viscosity of glycerol is about three orders of magnitude larger than that of water [44]. A spherical object of radius r in a viscous medium of dynamic viscosity η, at temperature T has an isotropic diffusion coefficient of

$$D = K_B T / 6\pi\eta r. \tag{7}$$

For a 6 nm spherical NP, and $\eta = 0.284$ Pa s at 313.15 K (40 °C) [45], the diffusion coefficient D in glycerol is $\sim 10^{-13}$ m^{2}s^{-1}, corresponding to a diffusion time of ~ 1 ms through a typical 10 nm plasma-liquid surface interface layer. Hence, particles that nucleate in the interface layer during the plasma on time can diffuse away from the interface towards the core of the droplet during the plasma off period. This transport removes the growing particles from the region where large densities of reducing electrons are available during the next pulse. During the power off time, Ag^+ from the bulk droplet can replenish the interface layer, resetting conditions for new particle nucleation during the next power on pulse. For our conditions, the bulk droplet is not depleted of Ag^+, and so the bulk droplet appears to be a continuous replenishing source to the surface layer. These processes are schematically shown in figure 8.

3.4. Structural integrity of glycerol

The preparation of silver NPs by a glycerol-based process was first reported by Sinha and Sharma, using silver nitrate as the metal precursor and glycerol as the solvent and reducing agent [46]. Two reduction mechanisms were proposed. Silver ions are reduced by (a) glyceraldehyde and dihydroxyacetone which are dehydration products of glycerol or (b) by alkoxide at high pH [47, 48]. To evaluate the glycerol chemical composition after plasma treatment, we performed FTIR spectroscopy, colorimetric aldehyde assay kit measurements, and pH measurements. The FTIR spectra of neat glycerol, plasma treated neat glycerol, AgNO$_3$-glycerol solution, and plasma treated AgNO$_3$-glycerol solution with and without pulse modulation are shown in figure 9. No additional peaks corresponding to the functional groups of glycerol by-products at 1650–1720 cm^{-1} [49, 50] were observed, which indicates that the structure of glycerol remained largely unchanged within the detection limit after plasma exposure. The peaks in the spectra at 1520–1550 cm^{-1} and 1262 cm^{-1} (figures 9(c)–(e)

Table 2. Four conditions used to study the relationship between nanoparticle size and plasma pulse parameters.

| Pulse frequency (Hz)	Duty cycle (%)	(Average) power (W)	Particle diameter (TEM) (nm)	Geometric standard deviation
—	100 (CW)	60	20.1	1.6
—	100 (CW)	12	14.9	1.4
10	20	12	9.1	1.3
100	20	12	5.6	1.4
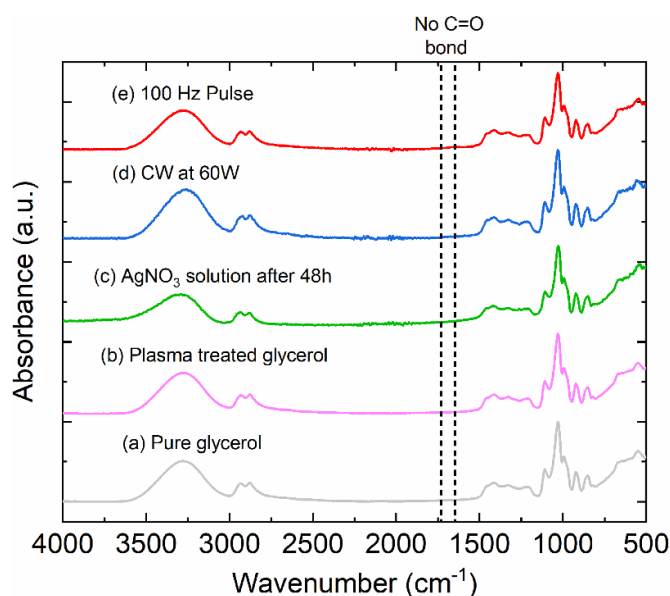
Figure 9. FTIR spectra of (a) neat glycerol, (b) plasma-treated glycerol without adding AgNO₃. The droplet residence time was 4 s with continuous plasma power of 60 W, (c) 10 mM AgNO₃ glycerol solution after mixing for 48 h, (d) as-synthesized colloidal dispersion at AgNO₃ initial concentration of 10 mM and 4 s residence time with plasma power of 60 W and (e) as-synthesized colloidal dispersion at AgNO₃ initial concentration of 10 mM and 4 s residence time with plasma pulsed power frequency of 100 Hz.

and S7) correspond to asymmetric stretching vibration ($\nu3$-NO$_3^-$) [51, 52].

To confirm the results of the FTIR spectroscopy, colorimetric assay kit measurements were performed for neat glycerol and plasma treated neat glycerol (figure S8). The aldehyde concentrations were both less than 100 μM before and after plasma treatment. These results indicate that glycerol did not decompose and produce significant amounts of glycolaldehyde for the experimental conditions. The lack of detecting significant glycolaldehyde may also eliminate aldehydes as acting as a reducing species for Ag$^+$. That said, there is the possibility that glycolaldehyde is produced and then rapidly consumed by reduction reactions (Ag$^+$ is not fully depleted).

H radicals have also been reported to be a strong reducing species of Ag$^+$ and relevant decomposition mechanisms were proposed for ethylene glycol [41, 53]. This reduction reaction is,

$$H + Ag^+ \rightarrow Ag^0 + H^+ \tag{8}$$
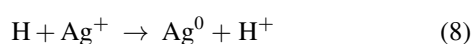
pH values of the solution (shown in table SI) actually slightly increased after plasma treatment. If the reduction of Ag$^+$ was dominated by H atoms, resulting in the production of H$^+$, one would expect acidification of the glycerol and a decrease in pH. Although H produced by dissociative processes of glycerol might make some minor contribution to reduction, the lack of significant fragmentation of glycerol and there being no reduction in pH suggest that H reduction is likely not important.

4. Conclusions

Surfactant-free spherical Ag NPs with narrow size distributions have been synthesized in a low pressure inductively coupled plasma reactor using droplets of a solution of AgNO₃ in glycerol. Two strategies were applied to control the size of Ag NPs—residence time of the droplet in contact with the plasma; and pulsed power modulation and plasma power. When the droplet residence time in contact with the plasma was reduced from 12 s to 4 s, NP diameter decreased and monodispersity of the size distribution improved. Employing pulsed power modulation to produce the plasma with a pulse frequency of 100 Hz produced particles with smaller sizes of $\sim$6 nm with a geometric standard deviation of 1.4, which we associated with a nucleation dominated regime resulting from the periodic production of finite inventories of Ag^0. Our measurements suggest that plasma-induced fragmentation of glycerol plays a minor role in the reduction of Ag$^+$ ions.

Data availability statement

All data that support the findings of this study are included within the article (and any supplementary files).

Acknowledgments

J. Phys. D: Appl. Phys. **55** (2022) 015201

C Xu *et al*

ORCID iDs

Chi Xu ⓘ https://orcid.org/0000-0002-3941-0512
Zichang Xiong ⓘ https://orcid.org/0000-0001-6486-1166
Mark J Kushner ⓘ https://orcid.org/0000-0001-7437-8573
Uwe R Kortshagen ⓘ https://orcid.org/0000-0001-5944-3656

References

[1] Saito G and Akiyama T 2015 *J. Nanomater.* **2015** 1–21
[2] Dupont J and Scholten J D 2010 *Chem. Soc. Rev.* **39** 1780
[3] Chen S, Carey J L, Whitcomb D R, Bühlmann P and Penn R L 2017 *Cryst. Growth Des.* **18** 324
[4] Ney A, Pampuch C, Koch R and Ploog K H 2003 *Nature* **425** 485
[5] McFarland A D and Van Duyne R P 2003 *Nano Lett.* **3** 1057
[6] Chen D, Qiao X, Qiu X and Chen J 2009 *J. Mater. Sci.* **44** 1076
[7] Rauwel P, Küünal S, Ferdov S and Rauwel E 2015 *Adv. Mater. Sci. Eng.* **2015** 682749
[8] Chandni, Andhariya N, Pandey O P and Chudasama B 2013 *RSC Adv.* **3** 1127
[9] Rumbach P and Go D B 2017 *Top. Catal.* **60** 799
[10] Chen Q, Li J and Li Y 2015 *J. Phys. D: Appl. Phys.* **48** 424005
[11] Bruggeman P J *et al* 2016 *Plasma Sources Sci. Technol.* **25** 053002
[12] Elg D T, Delgado H E, Martin D C, Sankaran R M, Rumbach P, Bartels D M and Go D B 2021 *Spectrochim. Acta B* **186** 106307
[13] Hofft O and Endres F 2011 *Phys. Chem. Chem. Phys.* **13** 13472
[14] Meiss S A, Rohnke M, Kienle L, Zein El Abedin S, Endres F and Janek J 2007 *Chem. Phys. Chem.* **8** 50
[15] Janiak C 2013 *Z. Naturforsch. B* **68** 1059
[16] Lazarus L L, Riche C T, Malmstadt N and Brutchey R L 2012 *Langmuir* **28** 15987
[17] Ullah M H, Il K and Ha C-S 2006 *Mater. Lett.* **60** 1496
[18] Ong H R, Rahman Khan M M, Ramli R, Du Y, Xi S and Yunus R M 2015 *RSC Adv.* **5** 24544
[19] Staszek M, Siegel J, Polívková M and Švorčík V 2017 *Mater. Lett.* **186** 341
[20] Maguire P, Rutherford D, Macias-Montero M, Mahony C, Kelsey C, Tweedie M, Perez-Martin F, McQuaid H, Diver D and Mariotti D 2017 *Nano Lett.* **17** 1336
[21] Holder C F and Schaak R E 2019 *ACS Nano* **13** 7359
[22] SigmaAldrich MAK140-1KT (available at: www.sigmaaldrich.com/US/en/product/sigma/mak140)
[23] Johnson E and Malter L 1950 *Phys. Rev.* **80** 58
[24] Chou Y, Talbot L and Willis D 1966 *Phys. Fluids* **9** 2150
[25] Bose S, Kaur M, Chattopadhyay P, Ghosh J, Saxena Y and Pal R 2017 *J. Plasma Phys.* **83** 615830201
[26] Kushner M J 2009 *J. Phys. D: Appl. Phys.* **42** 194013
[27] Tian P and Kushner M J 2017 *Plasma Sources Sci. Technol.* **26** 024005
[28] Tian P and Kushner M J 2015 *Plasma Sources Sci. Technol.* **24** 034017
[29] Evanoff D D and Chumanov G 2004 *J. Phys. Chem.* B **108** 13957
[30] Lee H, Park S H, Jung S-C, Yun J-J, Kim S-J and Kim D-H 2013 *J. Mater. Res.* **28** 1105
[31] Leng Z, Wu D, Yang Q, Zeng S and Xia W 2018 *Optik* **154** 33
[32] Bell F, Ruan Q N, Golan A, Horn P R, Ahmed M, Leone S R and Head-Gordon M 2013 *J. Am. Chem. Soc.* **135** 14229
[33] Ahmed M and Kostko O 2020 *Phys. Chem. Chem. Phys.* **22** 2713
[34] Martín A, Bordel N, Pereiro R and Bogaerts A 2008 *Spectrochim. Acta B* **63** 1274
[35] Alkaa A, Segur P, Zahraoui A and Kadri H M 1994 *Phys. Rev. E* **50** 3006
[36] Ellis H, Pai R, McDaniel E, Mason E and Viehland L 1976 *At. Data Nucl. Data Tables* **17** 177
[37] Kajiwara T and Thomas J 1972 *J. Phys. Chem.* **76** 1700
[38] Chiang W-H, Richmonds C and Sankaran R M 2010 *Plasma Sources Sci. Technol.* **19** 034011
[39] Mostafavi M, Marignier J, Amblard J and Belloni J 1989 *Int. J. Radiat. Appl. Instrum.* C **34** 605
[40] Henglein A 1989 *Chem. Rev.* **89** 1861
[41] Soroushian B, Lampre I, Belloni J and Mostafavi M 2005 *Radiat. Phys. Chem.* **72** 111
[42] Woehl T J, Evans J E, Arslan I, Ristenpart W D and Browning N D 2012 *ACS Nano* **6** 8599
[43] Loh N D, Sen S, Bosman M, Tan S F, Zhong J, Nijhuis C A, Kral P, Matsudaira P and Mirsaidov U 2017 *Nat. Chem.* **9** 77
[44] Rele M, Kapoor S, Sharma G and Mukherjee T 2004 *Phys. Chem. Chem. Phys.* **6** 590
[45] Segur J B and Oberstar H E 1951 *Ind. Eng. Chem.* **43** 2117
[46] Sinha A and Sharma B 2005 *Bull. Mater. Sci.* **28** 213
[47] Patel K, Kapoor S, Dave D P and Mukherjee T 2005 *J. Chem. Sci.* **117** 53
[48] Gomes J F, Garcia A C, Ferreira E B, Pires C, Oliveira V L, Tremiliosi-Filho G and Gasparotto L H 2015 *Phys. Chem. Chem. Phys.* **17** 21683
[49] Salehpour S and Dubé M A 2012 *Macromol. React. Eng.* **6** 85
[50] Balan V, Mihai C T, Cojocaru F D, Uritu C M, Dodi G, Botezat D and Gardikiotis I 2019 *Materials* **12** 2884
[51] Tran C T K, Tran H T T, Bui H T T, Dang T Q and Nguyen L Q 2017 *J. Sci.: Adv. Mater. Devices* **2** 172
[52] Ren H M, Cai C, Leng C B, Pang S F and Zhang Y H 2016 *J. Phys. Chem.* B **120** 2913
[53] Inwati G K, Rao Y and Singh M 2016 *Nanoscale Res. Lett.* **11** 458